Y.H. ZHAO[*]
J.Y. WANG[✉]
E.J. MITTEMEIJER

Microstructural changes in amorphous Si/crystalline Al thin bilayer films upon annealing

Max Planck Institute for Metals Research, Heisenbergstr. 3, 70569 Stuttgart, Germany

ABSTRACT Microstructural changes occurring in a sputter deposited Si (150 nm, amorphous)/Al (50 nm, crystalline); {111} fibre textured bilayer, upon annealing at 523 K for 60 min in a vacuum of 2.0×10^{-4} Pa, were analyzed employing X-ray diffraction, Auger electron spectroscopy, scanning electron microscopy, atomic force microscopy and focused-ion beam imaging. After the annealing the Al and Si sublayers had largely exchanged their locations in the bilayer; i.e. the Si layer was adjacent to the substrate after annealing. Simultaneously, the amorphous Si layer had crystallized into an aggregate of {111} oriented nanocrystals, with a crystallite size of about 15 nm. The Al layer, now adjacent to the surface, had formed a uniformly net-shaped layer in association with an increase of the surface roughness. Upon this rearrangement, the already initially present Al {111} fibre texture had become stronger, the Al crystallites had grown laterally and the macrostress in the Al layer had relaxed. An extensive analysis of thermodynamic driving forces for the transformation indicated that the largest gain in energy upon transformation is due to the crystallization of the amorphous Si. The only identifiable driving force for the layer exchange appears to be the release of elastic energy upon the rearrangement of the Si and Al phases in the layer.

PACS 61.43.D; 61.72.C; 62.40; 65.70; 68.55.J; 68.60.B

1 Introduction

A strong interest in reactions occurring in thin film systems exists, not only in view of the practical interest (e.g. the microelectronics industry [1–3]) but also because of great scientific interest: the thermodynamics and kinetics of thin film systems can differ dramatically from those for bulk systems, in particular because of the roles of the (high density of) interfaces and the internal stresses [4].

Against this background an interesting example of a semiconductor/metal system is the Si/Al system. According to the thermodynamics for bulk materials, Si and Al do not form compounds and are rather immiscible [5]. Such observations were obtained until now, upon annealing Si/Al bilayers. For Si/Al bilayers, where both sublayers are crystalline, abbreviated to c-Si/Al, it was found that the Al atoms diffuse through Si grain boundaries at temperatures as low as 573 K [6]; at higher temperatures (673–833 K), Si dissolves into Al followed by nucleation and growth of Si crystallites in the Al layer [7]. For Si/Al bilayers, where the Si layer is amorphous and the Al layer is crystalline, (abbreviated to a-Si/Al), various studies have shown that the presence of Al layer significantly lowers the crystallization temperature of a-Si as compared to bulk a-Si [8–10]. In situ transmission electron microscopy analysis of an a-Si/Al multilayer showed that, during annealing at 493 K, c-Si nucleates within the Al layers, and penetrates the Al as the c-Si grows [11, 12]. Annealing an a-Si/Al bilayer in a dry N_2 ambient (623–773 K) showed that c-Si nucleates at the Si/Al interface and grows further into the Al layer until, finally, a continuous c-Si film has formed at the initial Al layer [13–15].

In this study transformations occurring in a-Si/Al thin film systems were investigated, using in particular X-ray diffraction (XRD), Auger electron spectroscopy (AES), scanning electron microscopy (SEM), atomic force microscopy (AFM) and focused-ion beam (FIB) imaging. The effect of annealing at low temperature (523 K) was especially analyzed. A peculiar observation was made: the Si and Al sublayers (largely) exchanged their positions in the bilayer. The associated microstructural changes (crystallite size, microstrain, texture and stress) were extensively analyzed. A rigorous analysis of possible thermodynamic driving forces was given.

2 Experimental procedures

2.1 Specimen preparation and heat treatment

Commercially prepared, thermally oxidized, single crystalline (510)-oriented Si wafers, with a diameter of 100 mm and a thickness of 500 μm, were used as substrates. The thickness of the oxide layer was 50 nm. The Si (150 nm)/Al (50 nm) bilayer specimen was prepared by direct current magnetron sputter deposition from Al and Si targets (3 inch in diameter and purities of 99.999 wt. %) in an ultra-high vacuum (UHV) system at a base pressure of 10^{-7} Pa. The magnetron sputter apparatus has two exchangeable targets, enabling the preparation of the Si/Al bilayer specimen under vacuum in a single run. The magnetron beam axis was aligned with an angle of 22° with respect to the sub-

✉ Fax: +49-711/689-3312, E-mail: j.y.wang@mf.mpg.de
*Current address: Los Alamos National Laboratory, MS G755, MST-STC, Los Alamos, NM-87545, USA

strate surface, and the distance of targets to substrate was about 10 cm. Before deposition, the substrate and the targets were cleaned by argon ion sputtering. Then, deposition of the Si/Al bilayer was carried out at room temperature under an input power of 100 W and an Ar working pressure of 4.0×10^{-1} Pa. The deposition rates of Al and Si were 11 nm/min and 6 nm/min, respectively, which were determined by thickness measurements after deposition. During sputtering, the substrate was placed on a rotating table in the chamber and its temperature increased from 293 to about 323 K.

The as-prepared Si/Al bilayer was isothermally annealed at 523 K for 60 min in a vacuum of 2.0×10^{-4} Pa. Cooling of the annealed sample occurred under vacuum with a cooling rate of 2 K/min.

Commercial coarse-grained polycrystalline Al powder (with purity of 99.999 wt. %, particle diameter less than 50 μm) was enclosed in an evacuated silica tube (1.3×10^{-3} Pa) and annealed at 423 K for 3 hours to remove the structural imperfections. The annealed Al powder without structural defects was used as the reference sample in the X-ray diffraction line-broadening analysis.

2.2 *Microstructural and compositional characterization*

2.2.1 X-ray diffraction (XRD). A Philips MRD diffractometer was employed to perform phase analysis and texture, residual stress, crystallite size and microstrain determinations. The diffractometer was equipped with an Eulerian cradle, a copper tube operating at 1.8 kW, X-ray lens and a secondary monochromator to select Cu K_α radiation. To analyze the phases present in the as-prepared and annealed Si/Al bilayers, diffraction patterns were recorded by performing continuous θ-2θ scanning from $2\theta = 10°$ to $120°$ (where 2θ is the diffraction angle) with a scan speed of 2θ equal to 0.08 °/min. To study the texture of the as-prepared and annealed Al sublayers, a ϕ step scan from $0°$ to $360°$ with a step size of $3°$ and a counting time of 12 s per step, for the {111} reflection of the Al layers, was performed at specimen tilt angles ψ from $0°$ to $90°$ in steps of $2°$. For the determination of macrostress, crystallite size and microstrain, θ-2θ step scans were performed for the Al{111} and Si{111} reflections at different ψ angles. The peak parameters (peak-maximum position, full width at half maximum and integral breadth) were then determined by fitting a Pearson VII function to the peaks in the measured diffraction patterns using Philips Profit 1.0c software.

2.2.2 Auger electron spectroscopy (AES). The compositional characterization of the as-prepared and annealed Si/Al bilayers was performed using a JEOL 7830 scanning Auger microscope at a base pressure below 8.0×10^{-8} Pa. A static primary electron beam of 10 keV and 20 nA was used. The samples were sputtered using an ion gun with 1 keV Ar$^+$ ion beams. The ion incidence angle was about $40°$ with respect to the normal to the sample surface. The sputtered and analyzed areas were about 1 mm $\times$ 1 mm and 10 μm $\times$ 10 μm, respectively. AES sputter-depth profiles of the samples were obtained employing the discontinuous ion sputtering mode. The Al (1396 eV), Si (1621 eV) and O (507 eV) Auger electron signals as a function of the sputtering time were quantified by applying the relative elemental sensitivity factors: $S_{Al} = 0.23$, $S_{Si} = 0.16$ and $S_O = 0.23$, with respect to the Auger electron signal of pure Ag (356 eV), which all were measured under the same experimental conditions by the present Auger microscope.

2.2.3 Focused-ion beam imaging (FIB), scanning electron microscopy (SEM) and atomic forced microscopy (AFM). FIB imaging was performed using a FEI 200 XP FIB microscope. A Ga$^+$ ion beam was accelerated towards the target sample by a voltage of 30 keV for generating the secondary electron images. The probe current density was set to be 15 pA, corresponding to a beam diameter of about 10 nm, by controlling the strength of the electrostatic lenses and adjusting the effective aperture sizes. Elements Al and Si as well as grains (crystalline Al in the annealed films) with different crystallographic orientations can be clearly distinguished because they show different (channeling) contrasts in the secondary electron images.

In order to obtain the cross-sectional FIB images, a high Ga$^+$ ion current beam was used to mill a trench of a few micrometers length and 1 μm width and depth on the specimen surface. The sidewall of the trench was then made perfectly vertical and smoothly polished in the subsequent milling step. Finally the sample was tilted $45°$ and the polished sidewall was visualized.

Cross-sectional SEM observations of the broken specimens were made using a JEOL SM-6300F microscope. The electron beam was accelerated by a voltage of 5 kV in a vacuum of 4×10^{-5} Pa. The specimens were tilted $10°$ with respect to the surface normal.

Surface topographies were measured by atomic force microscopy, using a Multimode Scanning Probe Microscope (Digital Instrument Inc.), which was operated in tapping mode. The TappingMode^{TM} AFM operates by scanning a tip attached to the end of an oscillating cantilever across the sample surface. The tip lightly "taps" on the sample surface with a constant oscillation during scanning. The vertical position of the tip at each (x, y) data point is recorded to form the topographic image of the sample surface.

3   Results and evaluation

3.1   *Phase analysis*

The XRD patterns of the as-prepared and annealed Si (150 nm)/Al (50 nm)/Si (510) bilayer specimens, as well as of the 'bare' thermally oxidized Si (510) substrate, are shown in Fig. 1a. The XRD patterns of the as-prepared Si/Al bilayer, after subtracting the XRD background as recorded from the thermally oxidized Si (510) substrate, are shown in Fig. 1b. The Si sublayer in the as-prepared Si/Al bilayer is amorphous. This is evidenced by the broad scattering peak at about $2\theta = 27°$, which is characteristic of a-Si (Fig. 1b). The Al sublayer exhibits a {111} fibre texture. After annealing, the a-Si layer had crystallized into polycrystalline Si. The crystalline Si shows a {111} texture, exhibited by $I_{\{220\}}/I_{\{111\}}$ and $I_{\{311\}}/I_{\{111\}}$ intensity ratios of the crystallized c-Si which are much smaller than
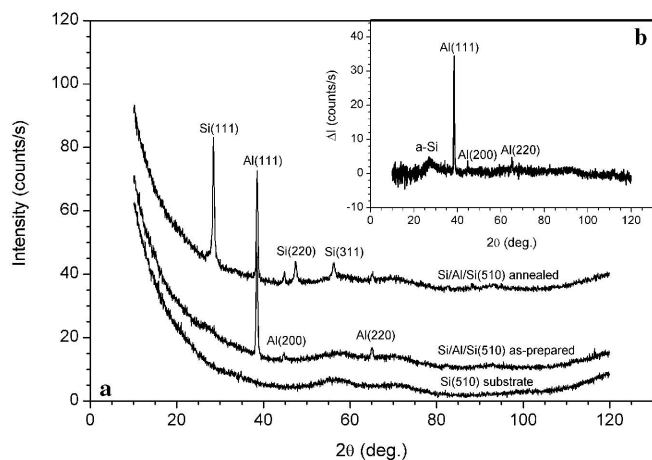
FIGURE 1 **a** XRD patterns of the as-prepared and annealed Si(150 nm)/Al(50 nm)/Si(510) bilayer specimens as well as of the 'bare' thermally oxidized Si(510) substrate. Vertical offsets have been applied to the individual patterns to avoid overlap. **b** XRD pattern of the as-prepared Si/Al bilayer after subtraction of the XRD background as recorded from the 'bare' Si (510) substrate

FIGURE 2 AES depth-profiles of the as-prepared (*solid symbols*) and annealed (*unfilled symbols*) Si(150 nm)/Al(50 nm)/Si(510) bilayer specimens

those given by the standard values on the ICDD-JCPDS card (no. 27-1402).

3.2 *Compositional and morphological analyses*

The AES depth profiles of the as-prepared and annealed Si (150 nm)/Al (50 nm)/SiO$_2$ (50 nm)/Si (510) bilayer specimens are shown in Fig. 2. The as-prepared Si/Al bilayer has a sharp interface between the outer a-Si layer and the inner crystalline Al layer. After annealing, most of the Si and Al layers have exchanged: most of the Al has moved to the surface and the Si has moved to the substrate. As follows from the O signal, no apparent compositional changes have occurred in the oxide (SiO$_2$) layer on top of the Si (510) substrate upon annealing.

Cross-sectional SEM pictures of the as-prepared and annealed Si/Al bilayers are shown in Fig. 3a and b. In the as-prepared state, three sublayers can be discerned: the SiO$_2$ layer on the top of the substrate and the Al and Si layers (Fig. 3a). The surface of the Si layer is smooth, and the Al layer is composed of crystallites. After annealing, most of
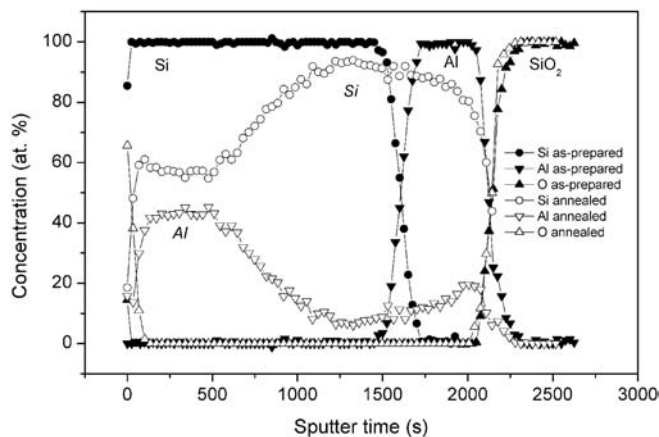
the Al grains are adjacent to the surface, and hillocks have formed on the surface of the layer (Fig. 3b). Energy dispersive X-ray spectroscopy (EDS) analysis indicated that the hillocks are Al.

The surface topographies of the as-prepared and annealed Si/Al bilayers are shown in Fig. 4a and b (AFM analysis). The surface of the as-prepared specimen is composed of small hills of about the same lateral size and height (Fig. 4a); after annealing, some relatively high (Al) mountains have grown on the surface (Fig. 4b), in agreement with the above discussed SEM observations. Upon annealing, the standard deviation of the height distribution of the Si/Al bilayer specimen increased from 3.5 nm to 5.2 nm.

Cross-sectional FIB micrographs of the as-prepared and annealed Si/Al bilayer specimens are shown in Fig. 5a and b. As in the case of the as-prepared bilayer, the Al layer and the Si layer can be clearly distinguished due to the difference in contrast in FIB microscopy (Fig. 5a). After annealing, most of the Al layer has moved upwards and has formed a uniform net-shaped structure on the surface (see the material of bright intensity in the upper and lower parts of Fig. 5b: at both sides of the milled trench the surface of the specimen is visualized (see Sect. 2.2.3)); most of the Si layer has moved downwards to the SiO$_2$ layer on top of the substrate (see the material of dark intensity in Fig. 5b). There are still some small Al grains
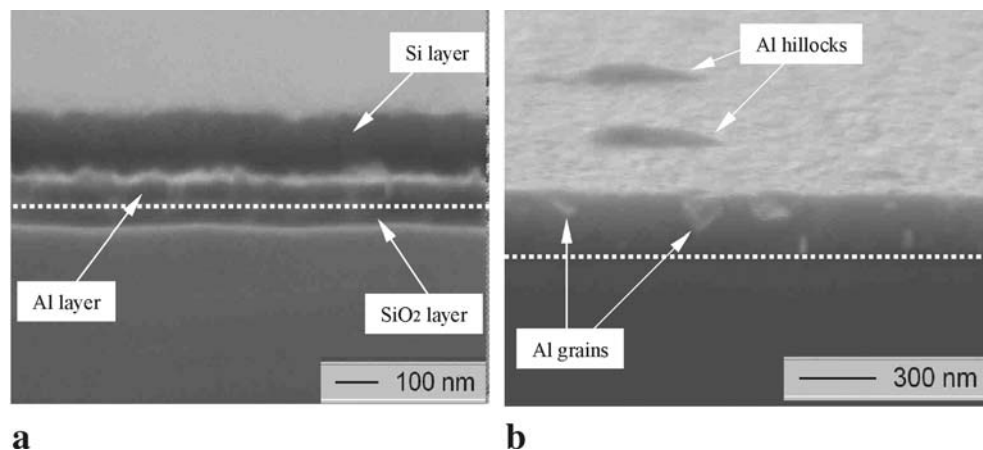

FIGURE 3 Cross-sectional SEM micrographs of the as-prepared (**a**) and annealed (**b**) Si/Al bilayers. The *white dotted lines* are guides to the eye for the interface between Al and SiO$_2$ sublayers of Fig. 3a, and for the interface between the annealed Si (Al) and SiO$_2$ layers of Fig. 3b. The seeming white layer between the Si and Al layers in the as-prepared condition is caused by the height difference induced during the process of breaking the specimen
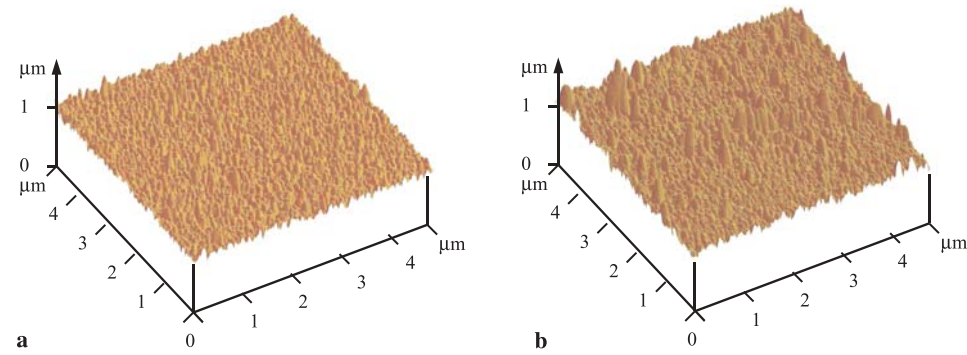
a   b

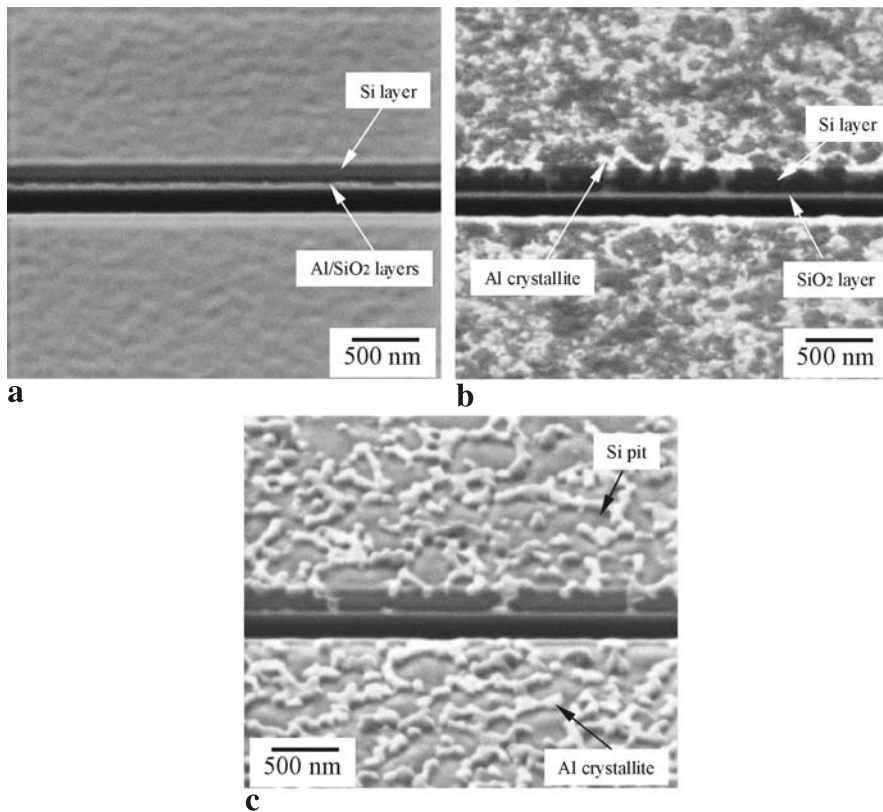a   b

c

FIGURE 5 Cross-sectional FIB micrographs of the as-prepared (**a**) and annealed (**b,c**) Si/Al bilayers. Figure 5c was taken at the same location as Fig. 5b but at a time 3 min later than Fig. 5b (i.e. 3 more minutes of Ga$^+$ ion sputtering). The middle parts of the micrographs are the cross-sectional FIB images (imaged sidewall of the trench milled (see Sect. 2.2.3), and the upper and the lower parts of the micrographs are the surface FIB images of the specimens

left at the interface between the Si and the SiO$_2$ layers. Thus, the FIB observations agree with the above discussed AES depth profiling results. In the FIB technique, a Ga$^+$ ion beam is used for generating the secondary electrons, which produce the image contrast. This ion beam results in the surface atoms of the specimens being sputtered away during the observation. The sputtering rate of Si is larger than that of Al and, therefore, the Si present at the imaged surface will be sputtered away faster than the Al. The FIB image taken at the same location as in Fig. 5b but at a time of about 3 min later is shown in Fig. 5c. It can be concluded from Fig. 5b and c that upon annealing Al has arrived at the surface of the specimen, and has enveloped the Si grains.

3.3   *Texture*

The Al {111} ψ scan and pole figures of the as-prepared and annealed Si/Al bilayers are shown in Fig. 6. Clearly, in both cases the Al sublayer exhibits a {111} fibre
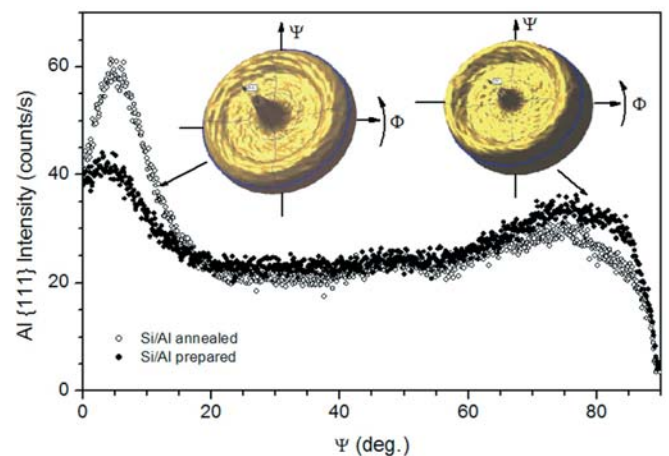

FIGURE 6 The ψ-dependences of the Al {111} peak intensities of the as-prepared (*solid circles*) and the annealed (*unfilled circles*) Si/Al bilayers. The *insets* represent the Al {111} pole figures for the as-prepared and annealed Si/Al bilayers

texture. The ψ-dependences of the Al {111} peak intensities of the as-prepared and annealed Si/Al bilayers indicate that after annealing, the Al {111} texture has become stronger.

3.4   *Residual stress analysis*

The Al {111} lattice strain, $\varepsilon_{\{111\}}^{Al}$, of the as-prepared (solid squares) and the annealed (unfilled squares) Si/Al bilayers, with reference to the (strain-free) lattice spacing, $d_{\{111\}}^0$, of standard Al powder ($d_{\{111\}}^0 = 2.338$ Å), is shown as function of $\sin^2 \psi$ in Fig. 7. For the cubic {111} fibre textured Al thin layer with a (proven by experiment) rotationally symmetric biaxial state of stress parallel to the surface, the lattice strain observed at specimen-tilt angle ψ, ε_ψ, can be related to the stress parallel to the surface in the Al, σ_1, by [16]:

$$\varepsilon_\psi^{\{111\}} = \left(2s_{12} + \frac{1}{2}s_{44}\sin^2\Psi + \frac{2}{3}s_0\right)\sigma_1 \tag{1}$$

where $s_0 = s_{11} - s_{12} - s_{44}/2$, with s_{11}, s_{12} and s_{44} as the elastic compliances of the single crystal Al, equal to 16.0 TPa^{-1}, -5.8 TPa^{-1} and 35.3 TPa^{-1}, respectively [17]. Hence, a plot of ε_ψ vs $\sin^2\psi$ yields a straight line, and σ_1 can be obtained from its slope. Thus it follows from Fig. 7 that the Al layer of the as-prepared specimen possesses a compressive stress parallel to the surface: $\sigma_1 = -139$ MPa, and that after annealing, the stress parallel to the surface of the Al layer has changed from compressive to tensile: $\sigma_1 = +182$ MPa.

Assuming that plastic deformation during the fast heating up can be neglected, at the beginning of annealing at 523 K, the macrostress of the Al layer parallel to the surface includes two components: one is the initial growth stress prevailing at room (deposition) temperature (-139 MPa); the other is the thermal stress due to the difference in thermal expansion, between substrate and Al layer, developing upon heating from room temperature to the annealing temperature. Because the substrate is much thicker than the layer, it can be assumed that all thermal misfit is accommodated by the Al layer. Then the thermal stress at the annealing temperature, σ_{th}, in the Al layer
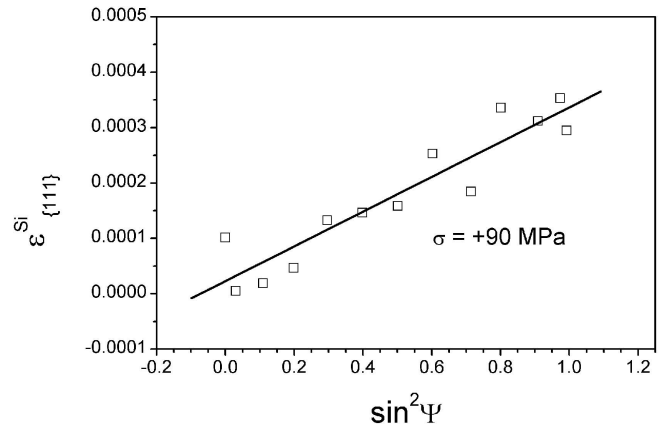
FIGURE 8   The Si {111} lattice strain, $\varepsilon_{\{111\}}^{Si}$, of the annealed Si/Al bilayer, with reference to the strain-free lattice spacing of standard Si powder, $d_{\{111\}}^0$, taken from ICDD-JCPDS card no. 27–1402, versus $\sin^2\psi$

can be calculated by:

$$\sigma_{th} = \frac{E_{\langle Al\rangle}}{1-\nu}(\alpha_{\langle Si\rangle} - \alpha_{\langle Al\rangle})(T_{annealing} - T_{room}) \tag{2}$$

where $\alpha_{\langle Al\rangle}$ and $\alpha_{\langle Si\rangle}$ are the linear coefficients of thermal expansion for c-Al and c-Si, equal 25×10^{-6} K^{-1} and 3×10^{-6} K^{-1}, respectively [17]; $E_{\langle Al\rangle}$ and ν are Young's modulus and Poisson's ratio of Al, equal 70.6 MPa and 0.345, respectively [18]. $\sigma_{th}(523\text{ K}) = -545$ MPa and thus, at the beginning of the anneal at 523 K, $\sigma_1(523\text{ K}) = (-595 + (-139))$MPa $= -684$ MPa.

The observation of a tensile macrostress at room temperature can then be interpreted such that during the anneal at 523 K all compressive macrostress in the Al relaxed. Cooling after the anneal would lead to build up of tensile thermal stress (analogous to the above reasoning). Because the cooling (as compared to the heating up) is very slow (2 K/min; see Sect. 2.1) stress relaxation during cooling can be appreciable [16] and this explains that only a part of the maximal thermal stress due to cooling is observed after cooling (182 MPa vs. 545 MPa).

The lattice strain, $\varepsilon_{\{111\}}^{Si}$, as recorded for the c-Si in the annealed Si/Al bilayer, with reference to the (strain-free) lattice spacing $d_{\{111\}}^0$ of standard Si powder ($d_{\{111\}}^0 = 3.135$ Å; ICDD-JCPDS card no. 27–1402), is shown as function of $\sin^2\psi$ in Fig. 8. For the cubic {111} textured Si thin layer with a rotationally symmetric biaxial stress state, the stress parallel to the layer surface, σ_1, can be calculated from (1). Again, the lattice strain ε_ψ versus $\sin^2\psi$ should yield a straight line. As follows from Fig. 8, here the straight line fitted to the data points in the $\varepsilon_{\{111\}}^{Si} - \sin^2\psi$ plot has a positive slope, indicating that the crystallized c-Si is subjected to a tensile stress. For the single crystal Si, s_{11}, s_{12} and s_{44} are 7.74 TPa^{-1}, -2.16 TPa^{-1} and 12.60 TPa^{-1}, respectively [17]. Accordingly, the stress parallel to the layer surface in the c-Si layer is $\sigma_1 = +90$ MPa.
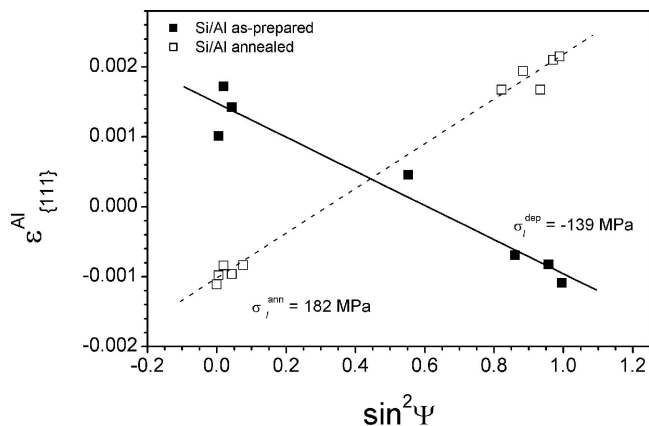

FIGURE 7   The Al {111} lattice strain, $\varepsilon_{\{111\}}^{Al}$, of the as-prepared (*solid squares*) and annealed (*unfilled squares*) Si/Al bilayers, with reference to the strain-free lattice spacing of standard Si powder, $d_{\{111\}}^0$, recorded from a standard Al powder, versus $\sin^2\psi$

3.5   *Crystallite size and microstrain analysis*

The measured diffraction-line profiles are the convolution of the structurally broadened profile of the specimen

with the instrumentally broadened profile [19]. The structurally broadened profile can originate from small crystallite size (often modeled with a Lorentzian broadening function) and/or microstrain (often modeled with a Gaussian broadening function). Here the instrumental broadening for the Al reflections was measured from a coarse-grained Al powder reference sample that did not exhibit significant structural broadening (see Sect. 2.1). On this basis, here the single line Voigt method was used to determine values for the crystallite size and the microstrain in the direction of the diffraction vector (for details, see [19]).

The crystallite (grain) size and the microstrain of the Al (layer) in the as-prepared and annealed Si/Al bilayers are shown in Fig. 9a and b as a function of $\sin^2 \psi$ (ψ indicates the direction of the diffraction vector $\boldsymbol{H}$: $\psi = 0°$: $\boldsymbol{H}$ is perpendicular to the surface; $\psi = 90°$: $\boldsymbol{H}$ is parallel to the surface). It follows that for the as-prepared sample, the Al-grain sizes along the layer surface ($\psi = 90°$) and along the normal to the layer surface ($\psi = 0°$) are nearly equal (about 50 nm), and of value comparable to the Al layer thickness. After annealing, the Al-grain size has remained about the same in the direction perpendicular to the surface and has increased laterally to about 70 nm (see the sketch in Fig. 9a). For the as-prepared Si/Al bilayer, the microstrain along the layer surface ($\psi = 90°$) in the Al is smaller than perpendicular to the layer surface ($\psi = 0°$). After annealing, the microstrain in Al per-

FIGURE 10 The crystallite size **a** and the microstrain **b** versus $\sin^2 \psi$ for the Si layer in the annealed Si/Al bilayer

pendicular to the layer surface has relaxed and an isotropic state of microstrain in the Al layer has been established.

Similarly, the crystallite (grain) size and the microstrain of the c-Si (i.e. after annealing) can be calculated from the broadening of the Si {111} peaks; see Fig. 10a and b. The crystallite size of the c-Si is very small: it varies from 19 nm perpendicular to the layer surface ($\psi = 0°$) to 12 nm parallel to the layer surface ($\psi = 90°$). The microstrain of the c-Si is also small, as compared to the microstrain in the Al phase: the largest microstrain occurs perpendicular to the layer surface: 0.17% ($\psi = 0°$).

4   Thermodynamic driving forces

The peculiar observation of the exchange (largely) of the locations of the Al (bottom to top) and Si (top to bottom) sublayers may have a kinetic origin, a thermodynamic origin, or both. Often, unexpected transformations are thought to have kinetic causes. However, it has been shown that, for example, (i) the formation of amorphous reaction layers at interfaces and (ii) the formation of amorphous oxide layers on metal surfaces can have a thermodynamic origin, rather than a kinetic origin as has been usually thought [4, 20]. It follows that tiny energy difference can have a great effect on the microstructural development, which holds in particular for thin films. Therefore an extensive analysis is presented of energy changes occurring in the Si/Al bilayer upon transformation. On that basis a possible driving force for the layer exchange may be identified.
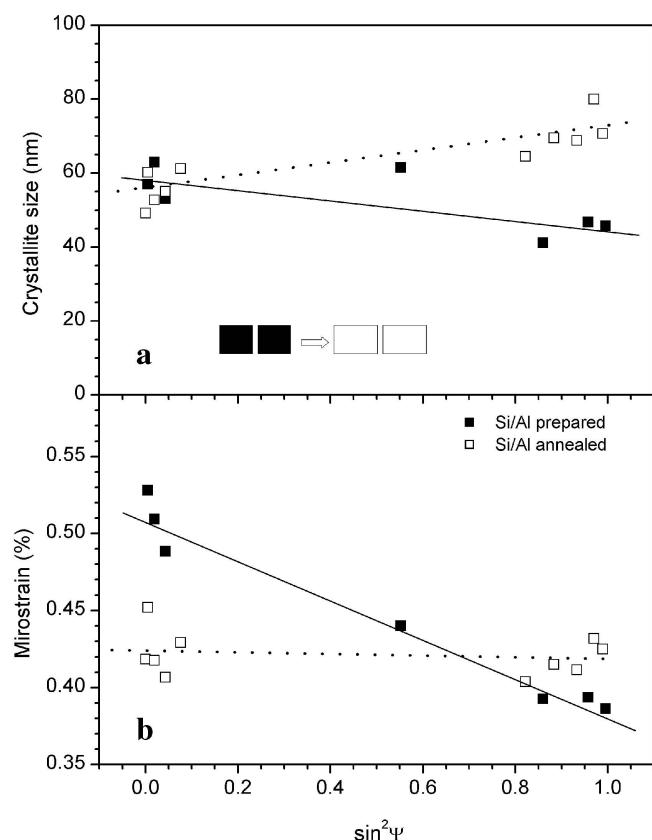

FIGURE 9 The crystallite size **a** and the microstrain **b** (for definitions, see [19]) versus $\sin^2 \psi$ for the Al layer in the as-prepared (*solid squares*) and annealed (*unfilled squares*) Si/Al bilayers. The sketch in **a** indicates that after annealing, the Al-grain size has remained the same in the direction perpendicular to the surface and has increased laterally
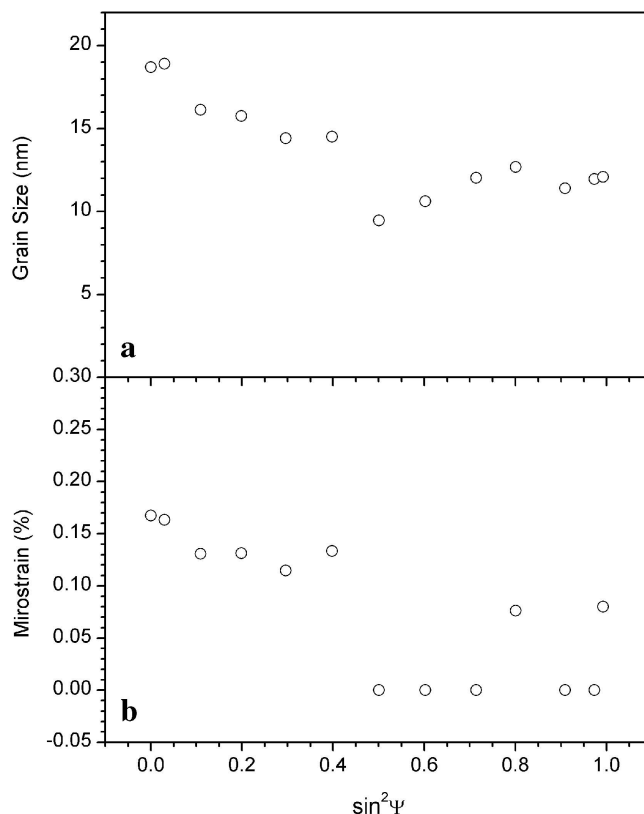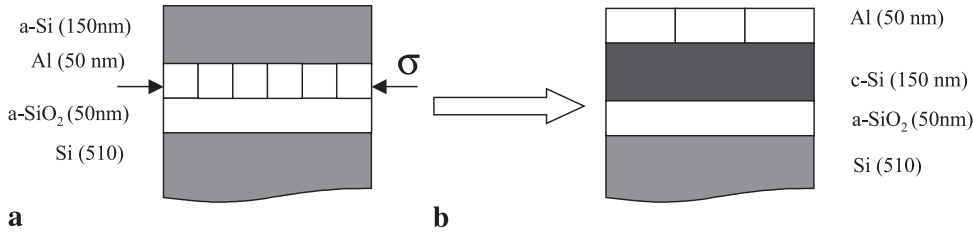
FIGURE 11 Schematic representation of the layer exchange occurring upon annealing the Si (150 nm)/Al (50 nm) bilayer. At the beginning of annealing at 523 K (**a**), the Si layer is amorphous, and the crystalline Al layer is subjected to a compressive macrostress and microstrain. At the end of annealing at 523 K (**b**), the Al and Si layers have largely exchanged their locations, a-Si has crystallized into {111} textured polycrystalline Si, the grain size of the Al has increased laterally and the macrostress and the microstrain of Al layer have been relaxed

A schematic representation of the transformation occurring upon annealing at 523 K in the initial Si (150 nm)/Al (50 nm) bilayer has been given in Fig. 11. The results presented in Sect. 3 can be summarized as follows. At the start of the annealing at 523 K (Fig. 11a), the Si layer is amorphous, and the Al layer is crystalline and subjected to a compressive macrostress and exhibits lattice distortions. At the end of the anneal at 523 K, the Al and Si layers have exchanged their locations, a-Si has crystallized into {111} oriented c-Si, the grains of the Al layer have grown laterally, and the (macro) stress and the microstrain in the Al layer have been relaxed completely and partially, respectively.

The Gibbs energy change of the bilayer per unit area parallel to the surface, ΔG, which has occurred at the end of annealing at 523 K as compared to the start of annealing at 523 K can be written as (see the treatment given in [4]):

$$\Delta G = D_{Si} \Delta G_{\langle Si \rangle - \{Si\}} + D_{Al} \Delta G_{Al}$$
$$+ (\gamma_{\langle Al \rangle} - \gamma_{\{Si\}}) + (\gamma_{\langle Al \rangle - \langle Si \rangle} - \gamma_{\langle Al \rangle - \{Si\}})$$
$$+ (\gamma_{\langle Si \rangle - \{SiO_2\}} - \gamma_{\langle Al \rangle - \{SiO_2\}}) \tag{3}$$

Here the symbol $\langle \rangle$ indicates the crystalline nature of a phase, and the symbol {} indicates the amorphous nature of a phase. The first term (written as ΔG_1) at the right-hand side of (3) is the Gibbs energy difference per unit area parallel to the surface between c-Si and a-Si; D_{Si} is the a-Si layer thickness, and $\Delta G_{\langle Si \rangle - \{Si\}}$ is the Gibbs energy difference between c-Si and a-Si at 523 K per unit volume. The second term (ΔG_2) at the right-hand side of (3) is the Gibbs energy change per unit area parallel to the surface between the annealed Al layer and the as-prepared Al layer; D_{Al} is the Al layer thickness, and ΔG_{Al} is the Gibbs energy difference between the annealed and unannealed Al layers per unit volume. The third term (ΔG_3) represents the difference in surface energy between crystalline Al (c-Al, $\gamma_{\langle Al \rangle}$) and a-Si ($\gamma_{\{Si\}}$). The fourth term ($\Delta G_4$) is the interface-energy difference between c-Al/c-Si ($\gamma_{\langle Al \rangle - \langle Si \rangle}$) and c-Al/a-Si ($\gamma_{\langle Al \rangle - \{Si\}}$). The 5th term ($\Delta G_5$) is the interface-energy difference between c-Si/a-SiO$_2$ ($\gamma_{\langle Si \rangle - \{SiO_2\}}$) and c-Al/a-SiO$_2$($\gamma_{\langle Al \rangle - \{SiO_2\}}$). This interfacial energy difference is about one order of magnitude smaller than the values of ΔG_3 and ΔG_4, since both a-SiO$_2$/c-Si and a-SiO$_2$/c-Al are solid ("crystalline")/liquid ("amorphous") interfaces. Therefore, ΔG_5 can be neglected.

4.1 Gibbs energy difference between c- Si and a- Si ($\Delta G_{\langle Si \rangle - \{Si\}}$), ΔG_1

The Gibbs energy difference between c-Si and a-Si, $\Delta G^{c-a}(T)$, can be estimated from the crystallization enthalpy, $-\Delta H^{c-a}(T_c)$, of a-Si at the crystallization temperature T_c:

$$\Delta G^{c-a}(T) = \Delta H^{c-a}(T) - T \Delta S^{c-a}(T)$$

$$\Delta H^{c-a}(T) = \Delta H^{c-a}(T_c) + \int_{T_c}^{T} \Delta c_p^{c-a} dT$$

$$\Delta S^{c-a}(T) = S_0^{c-a} + \int_{0}^{T} (\Delta c_p^{c-a}/T) dT \tag{4}$$

where $\Delta H^{c-a}(T)$, $\Delta S^{c-a}(T)$ and Δc_p^{c-a} are the differences in enthalpy, entropy and specific heat at constant pressure between c-Si and a-Si, respectively. S_0^{c-a} is the residual entropy difference between c-Si and a-Si at 0 K. This residual entropy difference was taken to be $-0.2 R$ (where R is the gas constant), which is an upper limit for the excess configurational entropy of an ideal four-coordinated random network [21]. For Δc_p^{c-a}, the following assumption was made [22]: $\Delta c_p^{c-a} = 0$ for $T < 78$ K, otherwise $\Delta c_p^{c-a} = (0.224 - 4.8T/1685)$ J/mol. This assumption uses the analytical fit to the Δc_p^{c-a} data for Ge [23] by replacing the value of the melting point of c-Ge (1210 K) by that of c-Si (1685 K). Since amorphous tetrahedral coordinated materials have a characteristic structure and intrinsic properties, independent of the preparation methods [22], the measured values for the negative of the heat of crystallization and the crystallization temperature of a-Si as-prepared by ion implantation [22] have been taken here: $\Delta H^{c-a}(T_c) = -11.9$ kJ/mol and $T_c = 960$ K.

Then, according to (4), $\Delta G^{c-a}(523 \text{ K}) = \Delta G_{\langle Si \rangle - \{Si\}}$ $(523 \text{ K}) = -10.16$ kJ/mol. Taking the mole volume of Si at 523 K equal to that at 300 K (12.1×10^{-6} m^3/mol [24]), it follows $\Delta G_1(523 \text{ K}) = -125.95$ J/m^2.

4.2 Gibbs energy change of Al layer, ΔG_2

The Gibbs energy change of the Al layer includes two components: energy release due to Al-grain growth,

ΔG_2^{gg}, and energy release due to relaxation of (macro) stress and microstrain, ΔG_2^{sm}.

4.2.1 Grain growth energy, $\Delta \mathbf{G}_2^{gg}$. The energy change due to Al-grain growth can be calculated from the Al grain-boundary (GB) energy $\gamma_{\langle Al \rangle}^{GB}$, and the reduction of the grain-boundary area ΔS^{gg}:

$$\Delta G_2^{gg} = \Delta S^{gg} \gamma_{\langle Al \rangle}^{GB} \tag{5a}$$

$\gamma_{\langle Al \rangle}^{GB}$ can be related to the temperature T by:

$$\gamma_{\langle Al \rangle}^{GB}(T) = \gamma_{\langle Al \rangle}^{GB,0} - T \frac{d\gamma_{\langle Al \rangle}^{GB}}{dT} \tag{5b}$$

where $\gamma_{\langle Al \rangle}^{GB,0}$ (Al GB energy at 0 K) and $d\gamma_{\langle Al \rangle}^{GB}/dT$ are 0.378 J/m^2 and 0.12 mJ/(m^2 K), respectively [25, 26]. Hence, $\gamma_{\langle Al \rangle}^{GB}(523 \text{ K}) = 0.348$ J/m^2.

For the (lateral) Al grain growth, as schematically shown in Fig. 9a (After annealing, the Al-grain size has remained the same in the direction perpendicular to the surface as the prepared sample and has increased laterally), ΔS^{gg} per unit area parallel to the surface can be calculated by:

$$\Delta S^{gg} = 2D_{Al} \left(\frac{1}{D_{ann.}} - \frac{1}{D_{unann.}} \right) \tag{5c}$$

where $D_{ann.}$ and $D_{unann.}$ are the grain sizes along the surface of the annealed and unannealed Al layers, here equal to 70 nm and 45 nm, respectively. According to (5a), (5b) and (5c), $\Delta G_2^{gg}(523 \text{ K}) = -0.28$ J/m^2.

4.2.2 Stress and microstrain release energy, ΔG_2^{sm}. According to the elasticity theory, the strain energy per unit volume, A_v, has the following relationship with all six components of stress (σ_x, σ_y, σ_z, τ_{xy}, τ_{yz}, τ_{xz}) or strain (ε_x, ε_y, ε_z, γ_{xy}, γ_{yz}, γ_{xz}) [27]:

$$2A_v = \frac{1}{E} \left[\sigma_x^2 + \sigma_y^2 + \sigma_z^2 - 2\nu(\sigma_y\sigma_z + \sigma_z\sigma_x + \sigma_x\sigma_y) \right.$$
$$\left. + 2(1+\nu)(\tau_{yz}^2 + \tau_{zx}^2 + \tau_{xy}^2) \right]$$
$$2A_v = (\lambda - 2\mu)(\varepsilon_x^2 + \varepsilon_y^2 + \varepsilon_z^2) + 2\lambda(\varepsilon_y\varepsilon_z + \varepsilon_z\varepsilon_x + \varepsilon_x\varepsilon_y)$$
$$+ \mu(\gamma_{yz}^2 + \gamma_{zx}^2 + \gamma_{xy}^2) \tag{6a}$$

where $\lambda = E\nu/[(1+\nu)(1-2\nu)]$, $\mu = E/[2(1+\nu)]$; with E as Young's modulus and ν as Poisson's ratio. For the Al thin layer subjected to an isotropic biaxial state of macrostress, σ_1, the strain energy per unit area parallel to the surface, A_a, can be given by:

$$A_a = D_{Al} \frac{1-\nu}{E} \sigma_1^2 \tag{6b}$$

It can be assumed that the stress in the Al layer has relaxed entirely during the annealing at 523 K, i.e. during the transformation analyzed (see discussion in Sect. 3.4). Therefore, using (6b) with $E = 70.6$ GPa and $\nu = 0.345$ [28], the change of energy due to macrostress relaxation is calculated to be -0.22 J/m^2.

According to the diffraction-line broadening analysis, the microstrain in the perpendicular direction of the Al layer had decreased after annealing from 0.5% to 0.4%, whereas the microstrain in the lateral direction remained constant (see Sect. 3.5). Then, adopting the lateral and perpendicular directions as principal directions, application of (6a) and an equation analogous to (6b), allows calculation of the change of energy due to microstrain relaxation: -0.025 J/m^2.

Hence, $\Delta G_2^{sm} = (-0.22 - 0.025)\text{J/m}^2 = -0.25$ J/m^2, and $\Delta G_2 = \Delta G_2^{gg} + \Delta G_2^{sm} = -0.53$ J/m^2.

4.3   *Surface energy difference between c- Al and a- Si, $\Delta \mathbf{G}_3$*

The surface energy, γ, of a liquid ("amorphous") phase can be related to the temperature T by [28]:

$$(\gamma V^{2/3})_T = (\gamma V^{2/3})_0 + bT \tag{7a}$$

where V in $(\gamma V^{2/3})_T$ is the molar volume at T, $(\gamma V^{2/3})_0$ is a measure for the surface enthalpy and V in $(\gamma V^{2/3})_0$ is the molar volume at 0 K. For liquid Si, $(\gamma V^{2/3})_0$ is 0.480 mJ/mol [28]. b is a measure for the entropy, and can be calculated by:

$$b = \frac{(\gamma V^{2/3})_{T_m} - (\gamma V^{2/3})_0}{T_m} \tag{7b}$$

where T_m is the melting point. For liquid Si, $(\gamma V_m^{2/3})_{T_m}$ is 0.396 mJ/mol [28, 29]. Thus, $b = -0.50 \times 10^{-7}$ J/K. A value for $(\gamma V^{2/3})_{523 \text{ K}}$ for a-Si can now be estimated using (7a). Then, taking $V_{\{Si\}}(523 \text{ K}) = 11.01 \times 10^{-6}$ m^3/mol [28, 29], one arrives at the following value for the surface energy of a-Si at 523 K, $\gamma_{\{Si\}}(523 \text{ K}) = 0.918$ J/m^2.

The surface energy of a solid at arbitrary temperature can be estimated by [28]:

$$\gamma^T = \gamma^0 + \frac{d\gamma}{dT} T \tag{8}$$

where γ^0 is the surface energy at 0 K. For c-Al, $\gamma_{\langle Al \rangle}^0$ is 1.160 J/m^2 [28], and $d\gamma/dT = -0.18$ mJ/m^2 [30]. Hence, $\gamma_{\langle Al \rangle}(523 \text{ K}) = 1.066$ J/m^2. (Similarly, for c-Si, $\gamma_{\langle Si \rangle}^0$ is 1.25 mJ/mol [28] and $d\gamma dT = -0.15$ mJ/m^2 [30], and thus, $\gamma_{\langle Si \rangle}(523 \text{ K}) = 1.172$ J/m^2. This result is used in Sect. 4.4.1.)

Finally it is obtained: $\Delta G_3 = \gamma_{\langle Al \rangle} - \gamma_{\{Si\}} = 0.15$ J/m^2.

4.4   *Interfacial energy difference between a- Si/c- Al and c- Si/c- Al, $\Delta \mathbf{G}_4$*

4.4.1 Interfacial energy of c- Al/c- Si ($\gamma_{\langle Al \rangle - \langle Si \rangle}$). The energy of the c-Al/c-Si interface contains two contributions [31]: the chemical interaction of Al and Si at the interface, $\gamma_{\langle Al \rangle - \langle Si \rangle}^{interaction}$, and the strain due to the mismatch at the interface between the two adjacent lattices, $\gamma_{\langle Al \rangle - \langle Si \rangle}^{mismatch}$:

$$\gamma_{\langle Al \rangle - \langle Si \rangle} = \gamma_{\langle Al \rangle - \langle Si \rangle}^{interaction} + \gamma_{\langle Al \rangle - \langle Si \rangle}^{mismatch} \tag{9a}$$

The chemical interaction energy is equal to the interface enthalpy per unit area and can be estimated by [4, 20]:

$$\gamma_{\langle Al \rangle - \langle Si \rangle}^{\text{interaction}} = \frac{\Delta H_{\text{Al}in\text{Si}}^{\text{interface}}}{C_0 V_{\text{Al}}^{2/3}} \quad (9b)$$

where $\Delta H_{\langle Al \rangle - \{Si\}}^{\text{interface}}$ is the enthalpy increase due to additional of one mole $\langle Al \rangle$ atoms to an infinitely large reservoir of Si. C_0 is a constant depending on the shape of the Wigner-Seitz cell and can be taken, on average, as $\cong 4.5 \times 10^8$ [28, 29]. V_{Al} is the molar volume of Al.

The mismatch term can be related to the high angle GB energies of Al and Si by estimating the high angle GB energy to be 1/3 of the surface energy [32]:

$$\gamma_{\langle Al \rangle - \langle Si \rangle}^{\text{mismatch}} = \frac{1}{6}(\gamma_{\langle Al \rangle} + \gamma_{\langle Si \rangle}) \quad (9c)$$

where (see data given in Sect. 4.3) $\gamma_{\langle Al \rangle}(523\,\text{K}) = 1.066\,\text{J/m}^2$, $\gamma_{\langle Si \rangle}(523\,\text{K}) = 1.172\,\text{J/m}^2$.

4.4.2 Interfacial energy of c- Al/a- Si ($\gamma_{\langle Al \rangle - \{Si\}}$). The c-Al/a-Si interfacial energy contains three contributions [4, 20]:

$$\gamma_{\langle Al \rangle - \{Si\}} = \gamma_{\langle Al \rangle - \{Si\}}^{\text{enthalpy}} + \gamma_{\langle Al \rangle - \{Si\}}^{\text{entropy}} + \gamma_{\langle Al \rangle - \{Si\}}^{\text{interaction}} \quad (10a)$$

The enthalpy contribution, $\gamma_{\langle Al \rangle - \{Si\}}^{\text{enthalpy}}$, arises from the c-Al phase at the interface. The entropy contribution, $\gamma_{\langle Al \rangle - \{Si\}}^{\text{entropy}}$, arises from a-Si at the interface [4]. The chemical interaction of Al and Si at the interface is described by $\gamma_{\langle Al \rangle - \{Si\}}^{\text{interaction}}$.

According to [29], $\gamma_{\langle Al \rangle - \{Si\}}^{\text{enthalpy}}$ is equal to a fixed fraction of the c-Al melting enthalpy $\Delta H_{\langle Al \rangle}^{\text{m}}$:

$$\gamma_{\langle Al \rangle - \{Si\}}^{\text{enthalpy}} = 2.5 \times 10^{-9} \frac{\Delta H_{\langle Al \rangle}^{\text{m}}}{V_{\langle Al \rangle}^{2/3}} \quad (10b)$$

where $V_{\langle Al \rangle}$ is the molar volume of the c-Al at the melting point ($= 10.50 \times 10^{-6}\,\text{m}^3/\text{mol}$ [28, 29]). $\Delta H_{\langle Al \rangle}^{\text{m}}$ equals 10.79 kJ/mol [23].

By eliminating the effect of a difference in molar surface area of c-Al and a-Si, $\gamma_{\langle Al \rangle - \{Si\}}^{\text{entropy}}$ can be estimated by the following empirical equation [32]:

$$\gamma_{\langle Al \rangle - \{Si\}}^{\text{entropy}} = 0.52 \times 10^{-7} \frac{T}{V_{\{Si\}}^{2/3}} \quad (10c)$$

with T in K and $V_{\{Si\}}$ is the molar volume of the liquid Si at the melting point: $V_{\{Si\}} = 11.01 \times 10^{-6}\,\text{m}^3/\text{mol}$ [28, 29].
$\gamma_{\langle Al \rangle - \{Si\}}^{\text{interaction}}$ can be represented by (9b).

Finally it is obtained: $\Delta G_4 = \gamma_{\langle Al \rangle - \langle Si \rangle} - \gamma_{\langle Al \rangle - \{Si\}} = 0.22\,\text{J/m}^2$.

5   General discussion of driving forces

The values of the different terms at the right-hand side of (3) have been gathered in Table 1. Clearly, ΔG_1 and ΔG_2 are negative, driving the transformation of the Si (150 nm)/Al (50 nm) bilayer system upon annealing, whereas

ΔG_1 (J/m^2)	ΔG_2 (J/m^2)	ΔG_3 (J/m^2)	ΔG_4 (J/m^2)	ΔG_5 (J/m^2)
-125.95	-0.53	0.15	0.22	0

TABLE 1   The calculated values for the Gibbs energy changes upon annealing the Si (150 nm)/Al (50 nm) bilayer at 523 K

ΔG_3 and ΔG_4 are positive and thereby counteract the transformation of the Si/Al bilayer.

The largest contribution to the driving force for the transformation is of course due to the crystallization of the amorphous Si. However, this driving force contribution cannot explain why layer exchange occurs. The calculations performed show that the changes in surface and interface energies also do not promote the layer exchange. One may suggest that kinetics is responsible for the layer exchange: agents for initiating the crystallization of the amorphous Si are sought, for example in the grain boundaries in the crystalline Al phase [33]. However, such a mechanism does not necessarily lead to layer exchange as observed, also it has to be considered likely that other heterogeneities, e.g. the free surface, do not facilitate initiation of crystallization. Therefore, an alternative explanation for the layer exchange is suggested. The layer exchange may be driven by the relaxation of elastic strain energy associated with the macrostress and the microstrain (ΔG_2) due to the drastic atomic rearrangement within the bilayer by the layer exchange, the misfit experienced in the initial, unannealed condition can be relieved. Here it should be noted, that in the above treatment, changes in strain energy for the Si phase were not taken into account. The measurement technique used (XRD) cannot be applied to the initial amorphous phase. Data obtained for the crystallized Si phase (see Sect. 3.4 and 3.5) indicate a low microstrain and a small intrinsic macrostress (because the substrate is a Si wafer, no thermal stress development upon heating and cooling is expected for the Si phase in the bilayer). Therefore it appears likely that ΔG_2 in any case is negative. Hence, it is suggested that the unfavorable changes in surface and interface energies upon layer exchange are overcompensated by the favorable changes in elastic energy.

6   Conclusion

Upon annealing of an a-Si/Al bilayer at 523 K the Si and Al largely exchanged their positions. The initially surface adjacent, amorphous Si, moved in the direction of the substrate and crystallized into {111} oriented nanocrystals with a small microstrain and a tensile macrostress parallel to the layer surface; the Al moved upwards in association with increases of the surface roughness, the strength of the {111} fibre texture and the lateral grain size, and release of macrostress and microstrain. Thermodynamic calculations for the transformation of the Si/Al bilayer upon annealing indicate that the largest gain in energy upon transformation is due to the crystallization of the amorphous Si. Changes in surface and interface energies counteract the layer exchange. The rearrangement of the Si and Al phases in the layer is promoted by the release of elastic strain energy.

REFERENCES

1   S.R. Herd, P. Chaudhari, M.H. Brodsky: J. Non-Cryst. Solids **7**, 309 (1972)
2   G. Ottaviani, D. Sigurd, V. Marrello, J.W. Mayer, J.O. McCaldin: J. Appl. Phys. **45**, 1730 (1974)
3   K. Nakamura, J.O. Olowolafe, S.S. Lau, M-A. Nicolet, J.W. Mayer, R. Shima: J. Appl. Phys. **47**, 1278 (1976)
4   R. Benedictus, A. Böttger, E.J. Mittemeijer: Phys. Rev. B **54**, 9109 (1996)
5   J.L. Murray, A.J. McAlister: Bull. Alloy Phase Diagrams **5**, 74 (1984)
6   K. Nakamura, M. Kamoshida: J. Appl. Phys. **48**, 5349 (1977)
7   K. Nakamura, M-A. Nicolet, J.W. Mayer, R.J. Blattner, C.A. Evans, Jr.: J. Appl. Phys. **46**, 4678 (1975)
8   F. Oki, Y. Ogawa, Y. Fujiki: Jpn. J. Appl. Phys. **8**, 1056 (1969)
9   J.R. Bosnell, U.C. Voisey: Thin Solid Films **6**, 161 (1970)
10 M.S. Haque, H.A. Naseem, W.D. Brown: J. Appl. Phys. **79**, 7529 (1996)
11 J.K. Toyohiko, S. Robert: Phil. Mag. B **66**, 749 (1992)
12 J.K. Toyohiko, S. Robert: Mater. Sci. Eng. A **179**/**180**, 426 (1994)
13 O. Nast, T. Puzzer, L.M. Koschier, A.B. Sproul, S.R. Wenham: Appl. Phys. Lett. **73**, 3214 (1998)
14 O. Nast, S.R. Wenham: J. Appl. Phys. **88**, 124 (2000)
15 O. Nast, A.J. Hartmann: J. Appl. Phys. **88**, 716 (2000)
16 A.C. Vermeulen, R. Delhez, Th.H. de Keijser, E.J. Mittemeijer: J. Appl. Phys. **77**, 5026 (1995)
17 E.A. Brandes, G.B. Brook: *Smithells Metals Reference Book*, 7th ed., (Butterworth-Heinemann Ltd, Oxford, 1992), p. 15–5
18 *CRC Handbook of Chemistry and Physics*, 65th ed., edited by R.C. Weast (CRC, Boca Taton, FL, 1984)
19 R. Delhez, T.H. de Keijer, E.J. Mittemeijer: Fres. Z. Anal. Chem. **312**, 1 (1982)
20 L.P.H. Jeurgens, W.G. Sloof, F.D. Tichelaar, E.J. Mittemeijer: Phys. Rev. B **62**, 4707 (2000)
21 F. Spaepen: Phil. Mag. **30**, 417 (1974)
22 E.P. Donovan, F. Spaepen, D. Turnbull, J.M. Poate, D.C. Jacobson: J. Appl. Phys. **57**, 1795 (1985)
23 H.S. Chen, D. Turnbull: J. Appl. Phys. **40**, 4214 (1969)
24 *Table of Periodic Properties of the Elements*, Sargent-Welch Scientific Company, Skokie, Illinois, 1980
25 H.V. Åstrom: Acta Met. **4**, 421 (1956)
26 L.E. Murr: Acta Met. **21**, 791 (1973)
27 S.P. Timoshenko, J.N. Goodier: *Theory of Elasticity*, 3rd ed. (McGraw-Hill Book Company Inc., New York, 1987)
28 F.R. de Boer, R. Boom, W.C.M. Mattens, A.R. Miedema, A.K. Niessen: *Cohesion in Metals*, (North-Holland, Amsterdam, 1988)
29 G. Lang: Z. Metallkd. **67**, 549 (1976)
30 A.R. Miedema: Z. Metallkd. **69**, 287 (1978)
31 D. Turnbull: Amer. Soc. Met. Ohio 121 (1955)
32 A.R. Miedema: F.J.A. den Broeder, Z. Metallkd. **70**, 14 (1970)
33 Y.H. Zhao, J.Y. Wang, E.J. Mittemeijer: to be published